Removal of Cr(VI) from water by a biochar-coupled g-C$_3$N$_4$ nanosheets composite and performance of a recycled photocatalyst in single and combined pollution systems

Kexin Li[a,b,1], Ziai Huang[a,1], Suiyi Zhu[a,b,*], Shenglian Luo[a], Liushui Yan[a], Yuhua Dai[a], Yihang Guo[b], Yuxin Yang[b]

[a] Key Laboratory of Jiangxi Province for Persistent Pollutants Control and Resources Recycle, NanChang Hangkong University, NanChang 330063, People's Republic of China
[b] School of Environment, Northeast Normal University, ChangChun 130117, People's Republic of China

ARTICLE INFO

ABSTRACT

A series of biochar-coupled graphitic carbon nitride nanosheets (BPCMSs/g-C$_3$N$_4$ NSs) composites was successfully fabricated through a simple two-step calcination strategy by using waste *Camellia oleifera* shells (WCOSs) and melamine as raw materials. Hexavalent chromium [Cr(VI)] or total chromium (T-Cr) in water could be completely removed or mostly recovered through adsorption combined with photocatalytic reduction by using the as-prepared BPCMSs/g-C$_3$N$_4$ NSs. The adsorbed Cr(VI) on BPCMSs/g-C$_3$N$_4$ NSs could be reduced by photogenerated electrons into trivalent chromium ions (Cr^{3+}) and stably fixed on BPCMSs/g-C$_3$N$_4$ NSs after strengthening. Interestingly, we found that the photocatalytic activity of the recycled Cr^{3+}/BPCMSs/g-C$_3$N$_4$ NSs was remarkably improved compared with that of the fresh BPCMSs/g-C$_3$N$_4$ NSs for the degradation of aqueous organic pollutants. We tested the photocatalytic performance of the recycled Cr^{3+}/BPCMSs/g-C$_3$N$_4$ NSs in the combined pollution system containing Cr(VI) and 4-fluorophenol (4-FP) and observed that a synergistic photocatalytic effect occurred in the Cr(VI)/4-FP combined pollution system under acidic and neutral conditions.

1. Introduction

With rapid social development, compounds containing Cr(VI) have been widely used in industrial production, such as electroplating, tanning, and pigment coloring [1–3]. Cr(VI)-containing compounds exposed to the environment enter natural waters through rainfall and wastewater discharge, causing persistent and serious harm to humans and other organisms [4–6]. Photocatalytic reduction is an effective strategy to remove Cr(VI) from water through photogenerated electrons produced by semiconductor photocatalysts because of various advantages, including low cost, high efficiency, and environmental protection [7–12]. However, some photocatalysts fail to satisfy the requirement of Cr(VI) reduction. Cr(VI) can be smoothly reduced by photogenerated electrons when the conduction band (CB) potential of a photocatalyst is more negative than the reduction potential of Cr(VI) [13–18]. Titanium dioxide (TiO$_2$)-based photocatalysts (e.g., SnS$_2$/TiO$_2$, Au/TiO$_2$-Pt, and Ag/Fe$_3$O$_4$/SiO$_2$/TiO$_2$) and some novel semiconductor photocatalysts (e.g., CuO/ZnO, MoS$_2$/Sb$_2$S$_3$, and Bi$_2$S$_3$/

Bi$_2$WO$_6$) have been used to reduce Cr(VI) in water [19–24]. Nevertheless, in practical applications, these photocatalysts exhibit some disadvantages, such as complex synthesis steps, poor stability, and lack of visible light response.

As a metal-free organic semiconductor photocatalyst with a good visible light response, graphitic carbon nitride (g-C$_3$N$_4$) has been widely applied to environmental photocatalysis [25–30]. In theory, Cr(VI) can be photocatalytically reduced by g-C$_3$N$_4$ under acidic conditions because the CB potential of g-C$_3$N$_4$ is more negative than the reduction potential of Cr(VI) [31–36]. However, the efficiency of the photocatalytic reduction of aqueous Cr(VI) by using g-C$_3$N$_4$ in practical applications is low because the bulk layered structure of g-C$_3$N$_4$ severely hinders the adequate contact of Cr(VI) with photogenerated electrons migrating to the photocatalyst surface [37–39]. The recycling of the reduced product trivalent chromium ions (Cr^{3+}) remaining in a photocatalytic system has been poorly investigated in studies on the photocatalytic reduction of aqueous Cr(VI); the photocatalytic reduction effect and mechanism of Cr(VI) in a combined pollution system have

---

also been rarely studied [40–43].

In this article, a series of biochar-coupled g-C$_3$N$_4$ nanosheets (BPCMSs/g-C$_3$N$_4$ NSs) composites is successfully fabricated through a simple two-step calcination strategy by using WCOSs and melamine as raw materials. The production cost of BPCMSs/g-C$_3$N$_4$ NSs is decreased by using low-cost raw materials and simple synthesis steps. Unlike conventional g-C$_3$N$_4$-based photocatalysts, the as-prepared BPCMSs/g-C$_3$N$_4$ NSs can completely remove Cr(VI) and mostly recover T-Cr from water through adsorption combined with photocatalytic reduction. Interestingly, Cr^{3+}/BPCMSs/g-C$_3$N$_4$ NSs are recycled after aqueous Cr(VI) is reduced, and their photocatalytic activity is remarkably increased compared with that of the fresh BPCMSs/g-C$_3$N$_4$ NSs toward aqueous organic pollutants degradation. Moreover, the recycled Cr^{3+}/BPCMSs/g-C$_3$N$_4$ NSs exhibit a stable photocatalytic performance in the 4-FP degradation photocatalytic system. The recycled Cr^{3+}/BPCMSs/g-C$_3$N$_4$ NSs also have a synergistic photocatalytic effect in the Cr(VI)/4-FP combined pollution system under acidic and neutral conditions. In particular, the reduction and degradation efficiencies of Cr(VI) and 4-FP simultaneously increase in the Cr(VI)/4-FP combined pollution system compared with that of the Cr(VI) or 4-FP single pollution system under acidic conditions. The total photocatalytic reaction rate of the Cr(VI)/4-FP combined pollution system is faster than that of the Cr(VI) or 4-FP single pollution system under neutral conditions. The mechanisms of the construction of BPCMSs/g-C$_3$N$_4$ NSs and recycled Cr^{3+}/BPCMSs/g-C$_3$N$_4$ NSs and the photocatalytic reactions in single or combined pollution systems are also discussed in detail.

2. Experimental

2.1. Chemicals and reagents

Waste *Camellia oleifera* shells (abbreviated WCOSs) were collected from Jiangxi Green Sea Oil Co., Ltd., China. Phloroglucinol (C$_6$H$_6$O$_3$, ≥ 99.0%) was purchased from Shanghai Macklin Biochemical Co., Ltd. Melamine (C$_3$H$_6$N$_6$, AR grade) was obtained from Tianjin Damao Chemical Reagent. Potassium dichromate (K$_2$Cr$_2$O$_7$, AR grade), 4-chlorophenol (C$_6$H$_5$OCl, GC grade, abbreviated 4-CP), 4-fluorophenol (C$_6$H$_5$OF, 99%, abbreviated 4-FP), and 4-nitrophenol (C$_6$H$_5$NO$_3$, GC grade, abbreviated 4-NP) were procured from Aladdin Chemistry Co., Ltd. Diphenylcarbazide (C$_{13}$H$_{14}$N$_4$O, AR grade) was bought from Sinopharm Chemical Reagent Co., Ltd.

2.2. Preparation

Bio-based porous carbon microspheres (BPCMSs) were prepared directly from WCOSs in accordance with our previous work [44]. In a typical synthesis, 1.6 g of WCOS powder and 0.4 g of phloroglucinol were uniformly dispersed in 60 mL of water by using a 500 W ultrasonic crasher for 1 h. The resulting suspension was stirred for 6 h at room temperature and then hydrothermally treated at 230 °C for 24 h at a heating rate of 1 °C/min. After centrifugation and drying were performed at 60 °C for 24 h, hydrothermal carbon was annealed at 650 °C for 2 h at a heating rate of 5 °C/min. Then, the annealed carbon and twice the mass of KOH were added in a beaker containing water and vigorously stirred at room temperature for 3 h. Afterward, the suspension was evaporated to dryness at 60 °C in a drying oven. Subsequently, the dry mixture was calcined at 850 °C for 2 h under an argon atmosphere with a heating rate of 5 °C/min and washed with water until a neutral pH was reached. Finally, the BPCMSs product was obtained.

For the preparation of BPCMSs/g-C$_3$N$_4$ NSs, 40, 80, 160, and 240 mg of BPCMSs and 1.6 g of melamine were uniformly dispersed into 60 mL of water by using a 500 W ultrasonic crasher for 30 min. After the mixture was stirred at room temperature for 6 h, the water in the suspension was removed through evaporation at 80 °C, and the dry mixture was calcined at 500 °C for 2 h under an argon atmosphere at a heating rate of 5 °C/min. The final biochar-coupled g-C$_3$N$_4$ nanosheets

composites were obtained and denoted as BPCMSs(*x*)/g-C$_3$N$_4$ NSs after the solid product was further calcined at 500 °C for 1 h under an air atmosphere at a heating rate of 5 °C/min, where *x* represents the added amount of BPCMSs during preparation. For comparison, pure g-C$_3$N$_4$ was prepared by subjecting melamine to direct polycondensation at 500 °C. Cr^{3+}/g-C$_3$N$_4$, Cr^{3+}/BPCMSs(40)/g-C$_3$N$_4$ NSs, Cr^{3+}/BPCMSs(80)/g-C$_3$N$_4$ NSs, and Cr^{3+}/BPCMSs(160)/g-C$_3$N$_4$ NSs were the recycled photocatalysts after aqueous Cr(VI) was adsorbed and photocatalytically reduced by using g-C$_3$N$_4$, BPCMSs(40)/g-C$_3$N$_4$ NSs, BPCMSs(80)/g-C$_3$N$_4$ NSs, and BPCMSs(160)/g-C$_3$N$_4$ NSs. Cr(VI)/BPCMSs(40)/g-C$_3$N$_4$ NSs were the recycled photocatalyst after Cr(VI) was adsorbed from water by using BPCMSs(40)/g-C$_3$N$_4$ NSs. All of the recycled photocatalysts were strengthened at 200 °C for 2 h and then washed thrice with water to ensure the stability of the recycled photocatalysts.

2.3. Characterizations

Field emission scanning electron microscopy (FESEM) images were recorded using Nova NanoSEM 450. Transmission electron microscopy (TEM) and high-resolution transmission electron microscopy (HRTEM) images were obtained using an FEI TalosF200X field emission transmission electron microscope. The elemental mappings of the samples were determined with an energy-dispersive X-ray (EDX) spectrometer equipped on TEM. Nitrogen gas porosimetry measurements were performed on a Quantachrome NOVA 2000e surface area and porosity analyzer after the samples were outgassed under vacuum at 70 °C for 20 min and 150 °C for 6 h. X-ray diffraction (XRD) patterns were obtained using a D8 ADVANCE diffractometer through Cu-*Kα* radiation. Fourier transform infrared (FTIR) spectra were obtained on a Nicolet iS5 FTIR apparatus. X-ray photoelectron spectra (XPS) were obtained using an Axis Ultra DLD instrument with a monochromated Al-*Kα* source at a residual gas pressure of less than 10^{-8} Pa. All of the binding energies were referenced to the C 1*s* peak at 284.8 eV of the surface adventitious carbon. UV–vis/diffuse reflectance spectroscopy (UV–vis/DRS) was conducted with a Lambda 750S UV/VIS/NIR spectrometer. Steady-state photoluminescence (PL) and time-resolved photoluminescence (TR-PL) measurements were carried out on an Edinburgh FS5 spectrofluorometer.

2.4. Photocatalytic tests

A PLS-SXE 300 Xe lamp (300 W, Beijing PerfectLight Co., Ltd., China) with an output wavelength (λ) of > 320 nm served as the simulated sunlight source. Visible light irradiation was obtained by removing UV irradiation from the lamp with a 420 nm cut filter, which could control λ at > 420 nm. Then, 50 mg of the photocatalyst and 50 mL of the reaction solution were poured into a 100 mL beaker with a quartz cover. The initial concentrations of Cr(VI), 4-CP, 4-FP, and 4-NP were 10 mg/L in the single and combined pollution systems. The acidic condition was set by adjusting the pH of the photocatalytic system to 2 with dilute H$_2$SO$_4$, and a neutral condition corresponded to the unadjusted pH of the photocatalytic system. The suspension was ultrasonicated for 10 min and stirred in the dark until the adsorption–desorption equilibrium was reached. Subsequently, the light source was switched on, and fixed amounts of the reaction solution were extracted at predetermined time intervals during irradiation. Changes in the Cr(VI) concentrations were analyzed via a diphenylcarbazide method by using a Lambda 750S UV/VIS/NIR spectrometer at λ of 540 nm. Changes in the T-Cr concentrations were detected using an Analytik Jena Contra AA 700 atomic absorption spectrometer. Changes in 4-CP, 4-FP, and 4-NP concentrations were examined using an Agilent 1100 series high-performance liquid chromatography (HPLC) with a C$_{18}$ column and a UV detector (λ = 280 nm for 4-CP and 4-FP, λ = 318 nm for 4-NP). Acetonitrile/water (60/40 *v/v*) was used as a mobile phase at a flow rate of 1.0 mL/min.
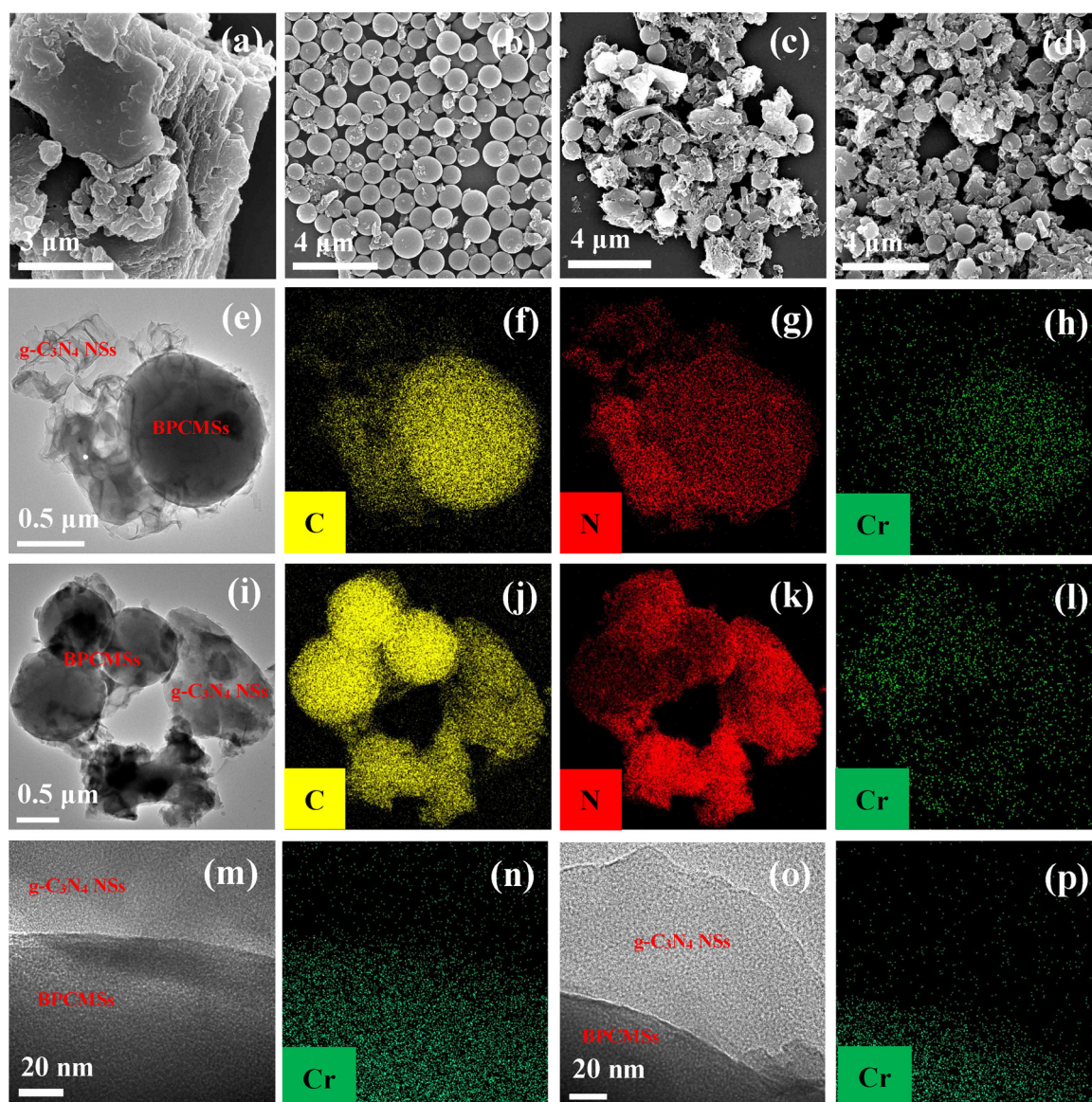
Fig. 1. FESEM images of as-prepared g-C$_3$N$_4$ (a), BPCMSs (b), BPCMSs(40)/g-C$_3$N$_4$ NSs (c), and BPCMSs(160)/g-C$_3$N$_4$ NSs (d); TEM images and corresponding C, N, and Cr EDX elemental mappings of recycled Cr^{3+}/BPCMSs(40)/g-C$_3$N$_4$ NSs (e–h) and Cr^{3+}/BPCMSs(160)/g-C$_3$N$_4$ NSs (i–l); HRTEM images and corresponding Cr EDX elemental mappings of recycled Cr^{3+}/BPCMSs(40)/g-C$_3$N$_4$ NSs (m and n) and Cr^{3+}/BPCMSs(160)/g-C$_3$N$_4$ NSs (o and p).

3. Results and discussion

3.1. Characterizations

3.1.1. Morphology and textural property

The morphological characteristics of the as-prepared materials were studied through FESEM, TEM, and HRTEM observation (Fig. 1). In Fig. 1a, the as-prepared g-C$_3$N$_4$ shows a bulk layered structure with more than five layers derived from the direct polycondensation of melamine at a high temperature. In Fig. 1b, a large amount of uniformly dispersed spherical microstructures can be observed in BPCMSs, although they undergo annealing at 650 °C and become chemically activated by KOH at 850 °C during preparation. Therefore, BPCMSs can be used as a dispersant during the high-temperature polycondensation of melamine because of the high thermal stability of BPCMSs. In Figs. 1c and d, BPCMSs and g-C$_3$N$_4$ nanosheets simultaneously exist in BPCMSs (40)/g-C$_3$N$_4$ NSs and BPCMSs(160)/g-C$_3$N$_4$ NSs, indicating that the addition of BPCMSs effectively inhibits the formation of bulk layered g-C$_3$N$_4$ during the high-temperature polycondensation of melamine.

Figs. 1e and i, the TEM images of the recycled Cr^{3+}/BPCMSs(40)/g-C$_3$N$_4$ NSs and Cr^{3+}/BPCMSs(160)/g-C$_3$N$_4$ NSs further demonstrate the successful construction of g-C$_3$N$_4$ nanosheets through the dispersion effect of BPCMSs during the high-temperature polycondensation of melamine. The corresponding EDX elemental mappings of the TEM images reveal that C, N, and Cr are present in the recycled Cr^{3+}/BPCMSs(40)/g-C$_3$N$_4$ NSs and Cr^{3+}/BPCMSs(160)/g-C$_3$N$_4$ NSs (Figs. 1f–h and j–l). Interestingly, the EDX elemental mappings in Figs. 1h and l show that Cr is mainly distributed on BPCMSs, indicating that the former is successfully captured by BPCMSs and stably fixed on BPCMSs after Cr(VI) is adsorbed and photocatalytically reduced and after strengthening is performed at 200 °C. The state of elemental Cr in the recycled photocatalysts was further determined through XPS. The interfacial contacts between different components in Cr^{3+}/BPCMSs/g-C$_3$N$_4$ NSs were further investigated through HRTEM observation. In Figs. 1m and o, the edges of BPCMSs and g-C$_3$N$_4$ nanosheets are closely connected without gaps, which can be attributed to the formation of chemical interactions between BPCMSs and g-C$_3$N$_4$ nanosheets during the simultaneous calcination of BPCMSs and melamine precursors. The
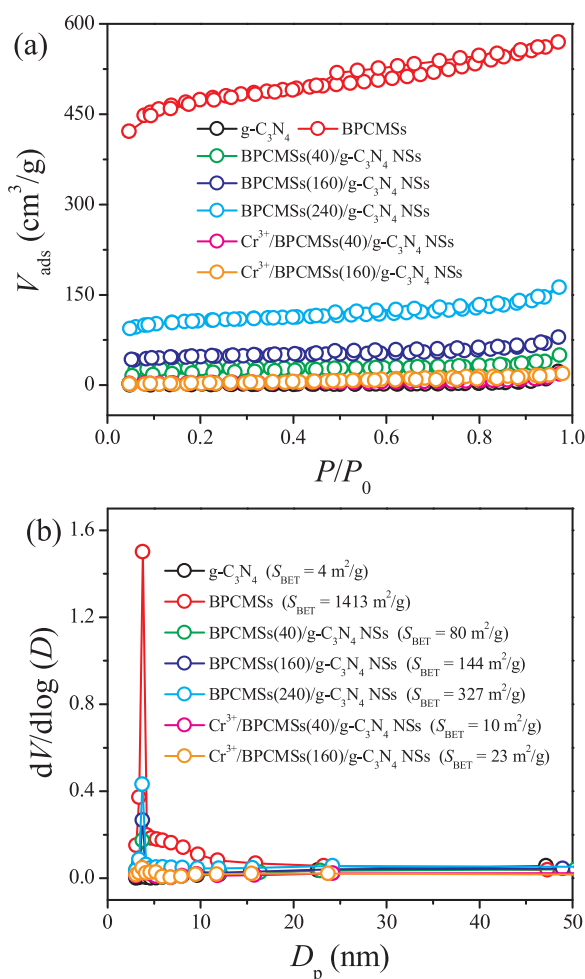
Fig. 2. Nitrogen gas adsorption-desorption isotherms (a) and pore-size distribution curves (b) of as-prepared materials.

Fig. 3. XRD patterns of as-prepared materials.

BPCMSs(40)/g-C_3N_4 NSs, BPCMSs(160)/g-C_3N_4 NSs, and BPCMSs (240)/g-C_3N_4 NSs further verify their mesoporous structures. The absence of the BJH pore size distribution peaks of Cr^{3+}/BPCMSs(40)/g-C_3N_4 NSs and Cr^{3+}/BPCMSs(160)/g-C_3N_4 NSs indicates that the pores on BPCMSs are blocked by Cr-containing compounds. The variations in the Brunauer–Emmett–Teller (BET) specific surface areas of all of the tested materials are consistent with the results of their adsorption capacities. Our pretest results reveal that all of the BET specific surface areas of BPCMSs/g-C_3N_4 NSs are less than $10 \, m^2/g$ in the absence of a further calcination step, suggesting that this step can effectively remove small g-C_3N_4 blocking the BPCMSs pores, thereby expanding the BET specific surface areas of BPCMSs/g-C_3N_4 NSs.

3.1.2. Compositional and structural information

The phase structures of the as-prepared materials were studied through wide-angle XRD in the range of 10°–80° (Fig. 3). For g-C_3N_4, the weak peak at 12.9° can be attributed to the diffraction of (100) plane with an in-plane structural packing motif period of 0.675 nm, whereas the strong peak at 27.1° is derived from the diffraction of (002) plane with $d = 0.33$ nm interlayer distance. The XRD peaks corresponding to BPCMSs cannot be observed because of their amorphous state. The XRD peaks of BPCMSs/g-C_3N_4 NSs corresponding to (100) and (002) planes are remarkably reduced compared with those of g-C_3N_4, indicating that the introduction of BPCMSs effectively prevents the formation of bulk layered g-C_3N_4 during high-temperature melamine polycondensation. The slightly decreased XRD peaks of the recycled Cr^{3+}/BPCMSs/g-C_3N_4 NSs compared with that of BPCMSs/g-C_3N_4 NSs suggest that a few characteristic planes of g-C_3N_4 nanosheets are covered by Cr-containing compounds.

The chemical structures of the as-prepared materials were studied on the basis of the FTIR spectra (Fig. 4). For g-C_3N_4, the sharp peak at 815 cm^{-1} can be attributed to the bending vibration of *s*-triazine units, a series of peaks in the range of 845–1904 cm^{-1} is derived from the stretching vibration of C—N and C=N in the CN heterocycles, and the broad peak centered at 3185 cm^{-1} corresponds to the stretching vibrations of primary (—NH_2) and secondary (=NH) amine groups. In comparison with the peaks of g-C_3N_4, the clearer FTIR characteristic absorption peaks of BPCMSs/g-C_3N_4 NSs and Cr^{3+}/BPCMSs/g-C_3N_4 NSs indicate that the successful construction of g-C_3N_4 nanosheets exposes more functional groups to the surface of the as-prepared composites. The FTIR characteristic absorption peaks corresponding to BPCMSs cannot be observed, suggesting that the fully graphitized BPCMSs with high thermal stability are obtained after they undergo hydrothermal carbonization, annealing, and KOH chemical activation.

The elemental composition and state of the as-prepared materials

corresponding EDX elemental mappings of the HRTEM images further confirm that Cr is mainly distributed on BPCMSs (Figs. 1n and p). However, Cr-related species cannot be observed in the HRTEM images shown in Figs. 1m and o, indicating that Cr is monodispersed in BPCMSs [45].

The textural properties of the as-prepared materials were studied on the basis of nitrogen gas adsorption–desorption isotherms and pore size distribution curves (Fig. 2). In Fig. 2a, the type II isotherm with an adsorption capacity close to zero corresponds to the nonporous bulk layered structure of g-C_3N_4. The type IV isotherm with a small H2-type hysteresis loop and a high adsorption capacity can be attributed to the small mesoporous structures of BPCMSs constructed through KOH chemical activation. The adsorption capacities of BPCMSs(40)/g-C_3N_4 NSs, BPCMSs(160)/g-C_3N_4 NSs, and BPCMSs(240)/g-C_3N_4 NSs are lower than that of BPCMSs because of the introduction of the g-C_3N_4 nanosheets component. However, the adsorption capacities of BPCMSs (40)/g-C_3N_4 NSs, BPCMSs(160)/g-C_3N_4 NSs, and BPCMSs(240)/g-C_3N_4 NSs gradually increase as the added amount of BPCMSs increases, indicating that the introduction of BPCMSs effectively improves the ability of the as-prepared BPCMSs/g-C_3N_4 NSs to capture nitrogen molecules. The adsorption capacities of the recycled Cr^{3+}/BPCMSs (40)/g-C_3N_4 NSs and Cr^{3+}/BPCMSs(160)/g-C_3N_4 NSs are lower than those of BPCMSs(40)/g-C_3N_4 NSs and BPCMSs(160)/g-C_3N_4 NSs, and this observation further confirms that Cr-containing compounds in the reaction system are successfully captured by BPCMSs and stably fixed on BPCMSs. In Fig. 2b, the narrow Barrett–Joyner–Halenda (BJH) pore size distribution peaks centered at approximately 3.7 nm for BPCMSs,
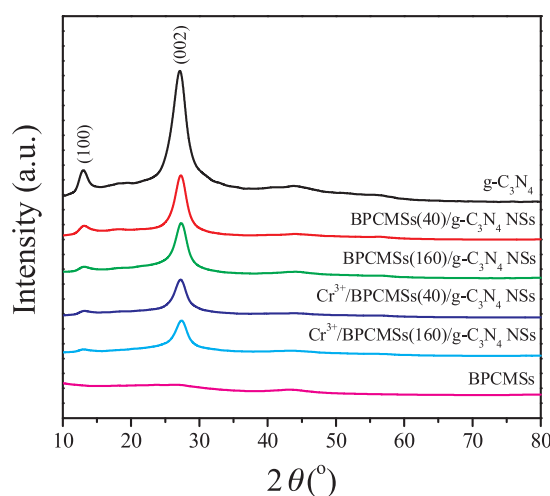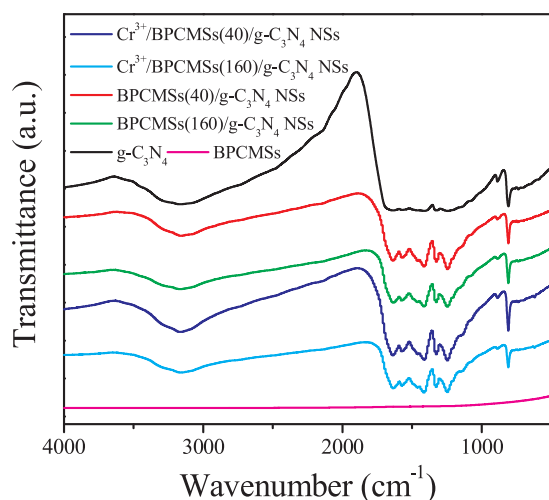
Fig. 4. FTIR spectra of as-prepared materials.

Fig. 5. High-resolution XPS of as-prepared materials in the C 1s (a), N 1s (b), and Cr 2p (c) binding energy regions.

were studied through high-resolution XPS in the C 1s, N 1s, and Cr 2p binding energy regions (Fig. 5). In Fig. 5a, BPCMSs show an obvious C 1s XPS peak centered at 284.8 eV, which is assigned to the C atoms in the C−C and C=C bonds that come from the graphitic and surface adventitious C. The relatively weak C 1s XPS peak centered at 285.7 eV in BPCMSs can be attributed to the C atoms in C−OH, which originate from KOH chemical activation. For g-C$_3$N$_4$, the C 1s XPS peak centered at 288.2 eV can be attributed to the sp^2-hybridized C atoms bonded to N in the aromatic ring (N=C−(N)$_2$). The C 1s XPS peak derived from N=C−(N)$_2$ slightly shifts to a higher binding energy for BPCMSs (40)/ g-C$_3$N$_4$ NSs and Cr(VI)/BPCMSs(40)/g-C$_3$N$_4$ NSs than for g-C$_3$N$_4$, indicating that the electronic environment of C atoms in N=C−(N)$_2$ is altered because of the formation of C−NH−C and/or C−O−C covalent bonds through the polycondensation between the surface C−NH$_2$ on g-C$_3$N$_4$ nanosheets and surface C−OH on BPCMSs. In comparison with the observations in BPCMSs(40)/g-C$_3$N$_4$ NSs and Cr(VI)/BPCMSs(40)/g-C$_3$N$_4$ NSs, the further shift of N=C−(N)$_2$ C 1s XPS peak to a higher binding energy for the recycled Cr^{3+}/BPCMSs(40)/g-C$_3$N$_4$ NSs indicates that the electron-withdrawing effect of Cr^{3+} further changes the electronic environment of C atoms in N=C−(N)$_2$. In Fig. 5b, the N 1s XPS peaks of g-C$_3$N$_4$ centered at 398.7, 399.9, and 401.3 eV can be attributed to the sp^2-hybridized aromatic N atoms bonded to C atoms (C=N−C), tertiary nitrogen groups [(C)$_3$−N] linking structural motifs (C$_6$N$_7$), or amino groups carrying hydrogen [(C)$_2$−NH, C−NH$_2$] in connection with structural defects and incomplete condensation and N atoms bonded to three C atoms in the aromatic cycles [N−(C)$_3$]. For BPCMSs(40)/g-C$_3$N$_4$ NSs and Cr(VI)/BPCMSs(40)/g-C$_3$N$_4$ NSs, the slight shift of the N 1s XPS peaks to a higher binding energy compared with that of g-C$_3$N$_4$ is due to the changed electronic environment of N atoms in the g-C$_3$N$_4$ nanosheets through the formation of C−NH−C and/or C−O−C covalent bonds. For the recycled Cr^{3+}/BPCMSs(40)/g-C$_3$N$_4$ NSs, the further shift of the N 1s XPS peaks to a higher binding energy compared with that of BPCMSs(40)/g-C$_3$N$_4$ NSs and Cr(VI)/ BPCMSs(40)/g-C$_3$N$_4$ NSs can also be attributed to the electron-withdrawing effect of Cr^{3+}, which further changes the electronic environment of N atoms in the g-C$_3$N$_4$ nanosheets. In Fig. 5c, the Cr 2p XPS peaks of Cr(VI)/BPCMSs(40)/g-C$_3$N$_4$ NSs centered at 579.3 and 588.7 eV are derived from Cr 2$p_{3/2}$ and Cr 2$p_{1/2}$ of Cr(VI) in Cr$_2$O$_7^{2-}$, and the Cr 2p XPS peaks of the recycled Cr^{3+}/BPCMSs(40)/g-C$_3$N$_4$ NSs centered at 576.8 and 587.3 eV can be attributed to Cr 2$p_{3/2}$ and Cr 2$p_{1/2}$ of Cr^{3+}. This result suggests that Cr^{3+} is successfully immobilized on the recycled Cr^{3+}/BPCMSs(40)/g-C$_3$N$_4$ NSs through the adsorption and photocatalytic reduction of aqueous Cr(VI) and the subsequent 200 °C strengthening step. In particular, Cr$_2$O$_7^{2-}$ in water is first adsorbed on the graphitized BPCMSs. Then, the photogenerated electrons produced
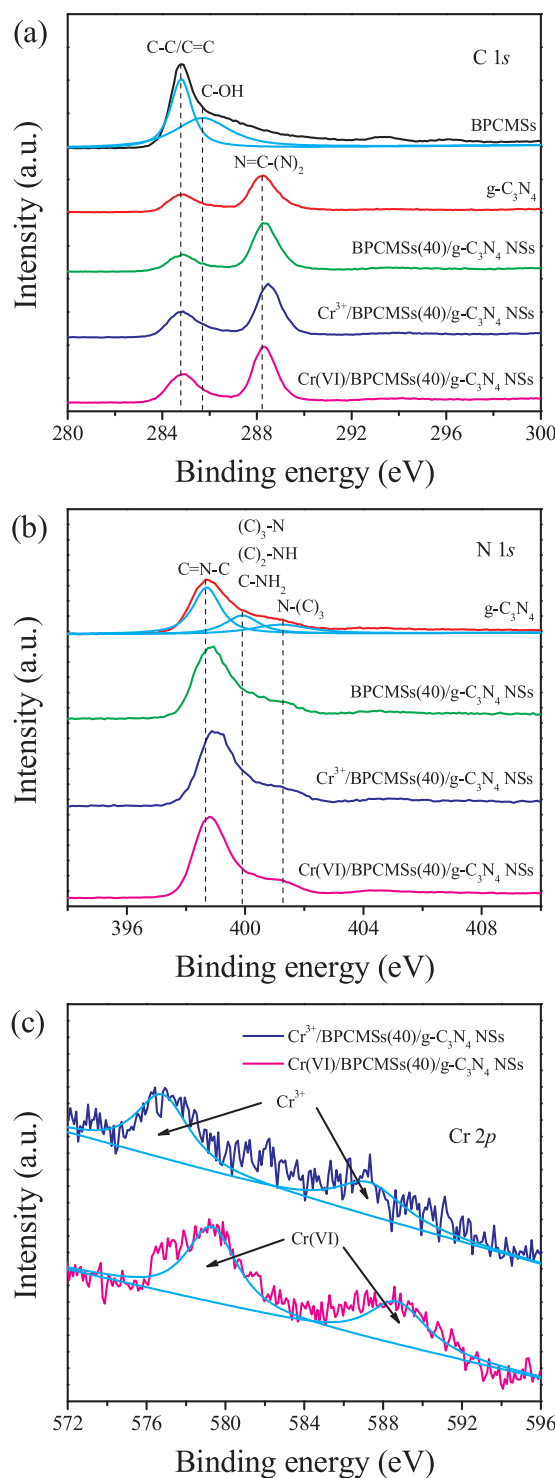
by the visible light excitation of g-C$_3$N$_4$ nanosheets are transferred to the graphitized BPCMSs through the electron conduction effect of the graphitized BPCMSs. Finally, Cr(VI) in Cr$_2$O$_7^{2-}$ is reduced to Cr^{3+} by the photogenerated electrons, and Cr^{3+} is stably fixed on BPCMSs by the electrostatic interaction with the surface C−OH after strengthening occurs at 200 °C (Scheme 1).

3.1.3. Optical and electronic properties

The light absorption properties of the as-prepared materials were
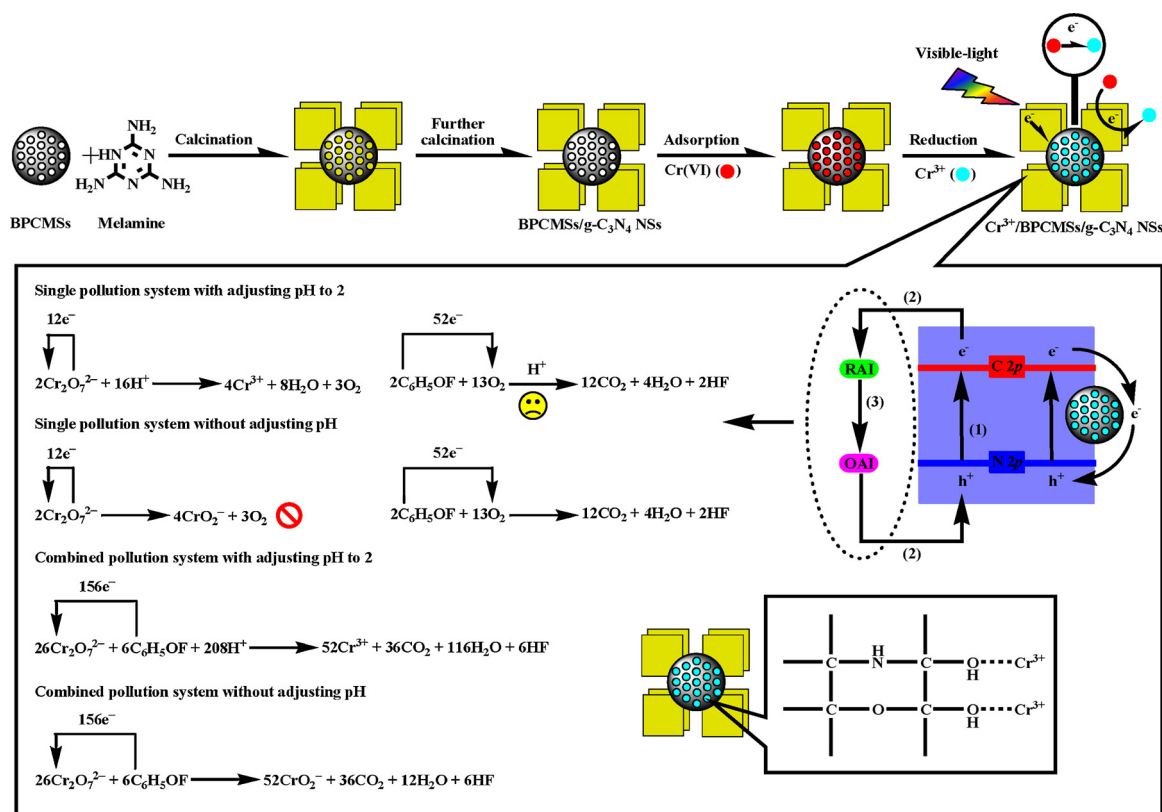
Scheme 1. The proposed fabrication route of BPCMSs/g-C_3N_4 NSs and recycled Cr^{3+}/BPCMSs/g-C_3N_4 NSs as well as the transfer of photogenerated electrons in different photocatalytic systems.
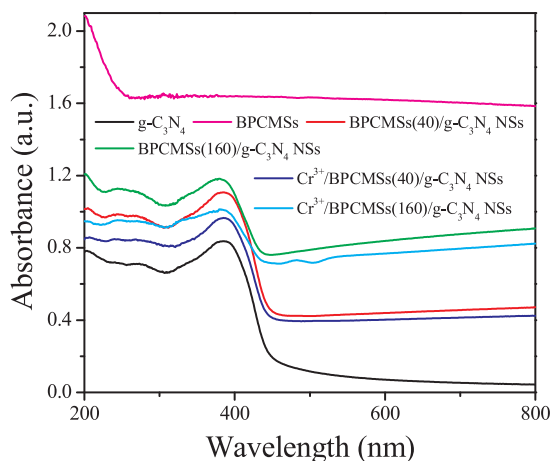

Fig. 6. UV–vis/DRS of as-prepared materials.

studied by UV–vis/DRS. In Fig. 6, g-C_3N_4 exhibits a characteristic semiconductor light absorption at 200–450 nm, which can be attributed to the electronic transition from the valence band (VB) populated by the N 2*p* orbit to the CB formed by the C 2*p* orbit. For the graphitized BPCMSs, the light absorption over the entire measured wavelength range is derived from the decreased reflectivity by the black graphitized BPCMSs [46]. In comparison with the light absorption of g-C_3N_4, the stronger light absorption of BPCMSs/g-C_3N_4 NSs at 200–450 nm suggests that the incident photons captured by BPCMSs enhance the electronic transition efficiency from VB to CB in the g-C_3N_4 nanosheets. The slightly weakened light absorption of the recycled Cr^{3+}/BPCMSs/g-C_3N_4 NSs relative to that of BPCMSs/g-C_3N_4 NSs at 200–450 nm indicates that the electron-withdrawing effect of Cr^{3+} slightly reduces the electronic transition efficiency from VB to CB in the g-C_3N_4 nanosheets.

The photocatalytic quantum efficiencies of the as-prepared materials were initially studied through PL measurements. In Fig. 7a, g-C_3N_4 shows a strong fluorescence emission peak at 400–700 nm, indicating that a large number of photoinduced e^-–h^+ pairs are generated and rapidly recombined within g-C_3N_4. In comparison with the peaks of g-C_3N_4, the fluorescence emission peaks of BPCMSs/g-C_3N_4 NSs gradually decrease as the added amount of BPCMSs increases, implying that the recombination of e^-–h^+ pairs is effectively suppressed by the construction of g-C_3N_4 nanosheets and the electron conduction effect of the graphitized BPCMSs. The shift of the fluorescence emission peaks of BPCMSs/g-C_3N_4 NSs relative to g-C_3N_4 can be attributed to the quantum size effect produced by the construction of g-C_3N_4 nanosheets [47]. In comparison with the peaks of BPCMSs/g-C_3N_4 NSs, the stronger fluorescence emission peaks of the recycled Cr^{3+}/BPCMSs/g-C_3N_4 NSs suggest that Cr^{3+} induces more photogenerated carriers to migrate to the surface of the g-C_3N_4 nanosheets via the electron-withdrawing effect. The lifetimes of the photogenerated carriers of the as-prepared materials were further studied through TR-PL measurements. In Fig. 7b and Table 1, the PL decay curves of the as-prepared materials are fitted by the bi-exponential kinetic function [$R(t) = B_1 \cdot \exp(-t/\tau_1) + B_2 \cdot \exp(-t/\tau_2)$], and two decay components, namely, τ_1 and τ_2, are derived. The short lifetime component (τ_1) usually originates from nonradiative relaxation related to material defects, whereas the long lifetime component (τ_2) can be attributed to radiation produced by the recombination of photogenerated carriers [48]. τ_2 of BPCMSs(40)/g-C_3N_4 NSs is longer than that of g-C_3N_4, implying that the construction of the g-C_3N_4 nanosheets and the electron conduction effect of the graphitized BPCMSs slow down the recombination of the photogenerated carriers. The longer τ_2 of Cr^{3+}/BPCMSs(40)/g-C_3N_4 NSs than that of BPCMSs(40)/g-C_3N_4 NSs suggests that the recombination rate of the photogenerated carriers is further slowed down by the electron-withdrawing effect of Cr^{3+}. As a representative of the overall decay behavior, the average PL lifetimes of g-C_3N_4, BPCMSs(40)/g-C_3N_4 NSs, and Cr^{3+}/BPCMSs(40)/g-
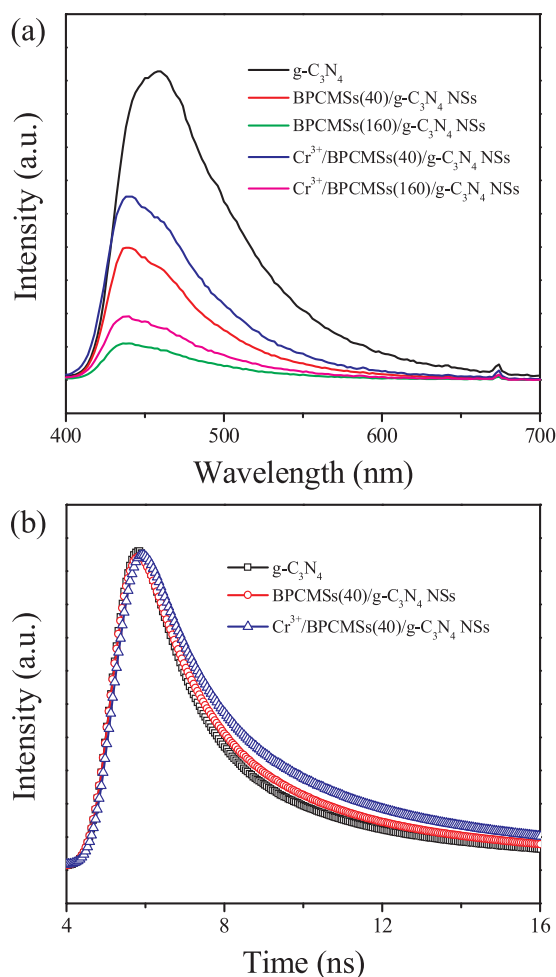
Fig. 7. PL (a) and TR-PL (b) spectra of as-prepared materials.

Table 1
The fitted fluorescence decay components of as-prepared photocatalysts.

Photocatalysts	τ_1 (ns)	τ_2 (ns)	Ave. τ (ns)
g-C$_3$N$_4$	1.404	6.255	3.8
BPCMSs(40)/g-C$_3$N$_4$ NSs	1.577	6.919	4.5
Cr^{3+}/BPCMSs(40)/g-C$_3$N$_4$ NSs	1.706	7.256	5.1

C$_3$N$_4$ NSs are 3.8, 4.5, and 5.1 ns, respectively (Table 1).

3.2. Photocatalytic tests

Conventional g-C$_3$N$_4$ photocatalysts can slowly reduce Cr(VI) to Cr^{3+} through visible light irradiation under acidic conditions, but Cr^{3+} cannot be further photocatalytically reduced by g-C$_3$N$_4$. Therefore, the removal of Cr(VI) from water by using g-C$_3$N$_4$ not only exhibits in-efficiency but also allows Cr^{3+} to persist in water. Cr^{3+} remaining in water is also toxic to organisms and can be easily oxidized again to Cr (VI) by oxidizing agents. On the basis of these problems, we developed a series of BPCMSs/g-C$_3$N$_4$ NSs composites to remove Cr(VI) and T-Cr from water effectively through adsorption combined with photo-catalytic reduction. Interestingly, Cr(VI) adsorbed on BPCMSs/g-C$_3$N$_4$ NSs is also reduced to Cr^{3+} by the photogenerated electrons, which further enhance the photocatalytic activity of BPCMSs/g-C$_3$N$_4$ NSs. We further investigated the photocatalytic performance of the recycled Cr^{3+}/BPCMSs/g-C$_3$N$_4$ NSs in the combined pollution system. The photocatalytic efficiency of the combined pollution system is re-markably improved compared with that of the single pollution system
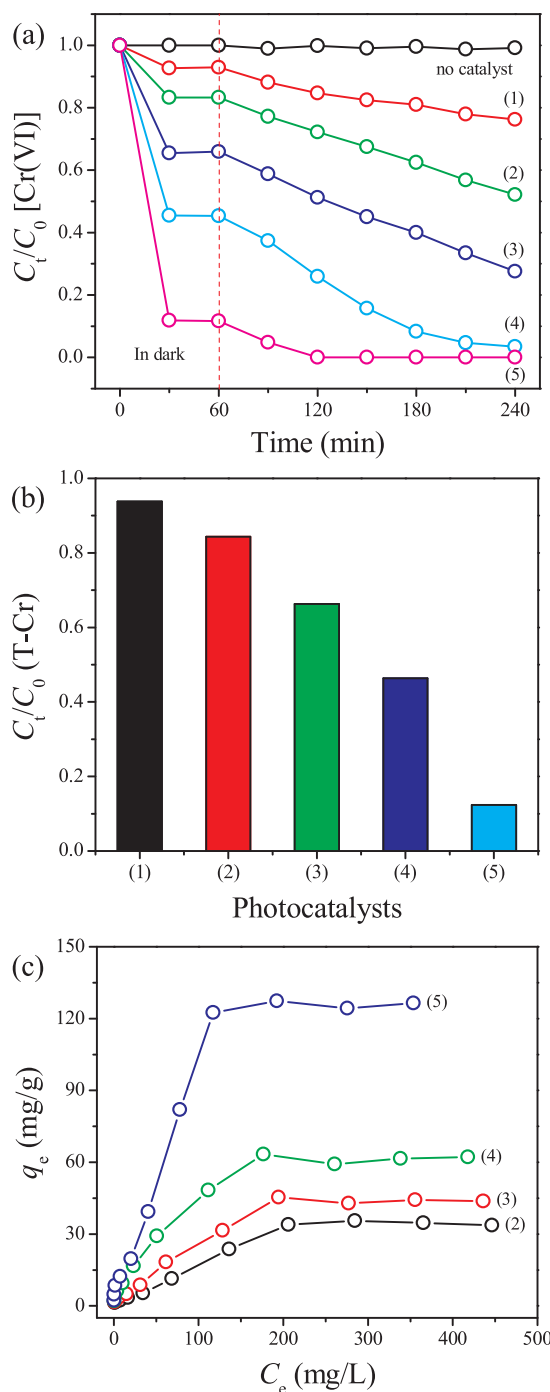

Fig. 8. Removal of Cr(VI) (a) and T-Cr (b) from water by adsorption combined with photocatalytic reduction and adsorption isotherms (c) of aqueous Cr(VI) on the as-prepared materials: g-C$_3$N$_4$ (1), BPCMSs(40)/g-C$_3$N$_4$ NSs (2), BPCMSs (80)/g-C$_3$N$_4$ NSs (3), BPCMSs(160)/g-C$_3$N$_4$ NSs (4), and BPCMSs(240)/g-C$_3$N$_4$ NSs (5).

because of the synergistic photocatalytic effects.

3.2.1. Removal of Cr(VI) and T-Cr from water by adsorption combined with photocatalytic reduction

Cr(VI) and T-Cr were removed from water through adsorption combined with photocatalytic reduction in an aqueous solution con-taining 10 mg/L Cr(VI) with pH adjusted to 2 by dilute H$_2$SO$_4$. In Fig. 8a, the blank test (no catalyst) shows that Cr(VI) in water cannot be reduced because of the lack of photogenerated electrons, and the ad-sorption–desorption equilibria between Cr(VI) and the as-prepared

materials are reached before visible light irradiation is administered. The adsorption capacity of g-C_3N_4 for Cr(VI) is less than 10% because of its small BET specific surface area, and the final removal rate of Cr(VI) is less than 25% after 3 h of visible light irradiation due to the rapid recombination of e^-–h^+ pairs within g-C_3N_4. The adsorption capacities of BPCMSs/g-C_3N_4 NSs for Cr(VI) monotonically increase as the added amount of BPCMSs increases from 40 mg to 240 mg, indicating that the introduction of BPCMSs effectively enhances the abilities of BPCMSs/g-C_3N_4 NSs to capture Cr(VI) because of the large BET specific surface area of BPCMSs. The final removal rates of Cr(VI) from water by using BPCMSs/g-C_3N_4 NSs also monotonically increase as the added amount of BPCMSs increases, suggesting that the effective capture of Cr(VI) and the construction of g-C_3N_4 nanosheets significantly increase the reduction probability of Cr(VI) via the photogenerated electrons.

To further study the removal effect of T-Cr from water, we tested the content of T-Cr in the reaction solution after 3 h of visible light irradiation by using an atomic absorption spectrometer (Fig. 8b). The removal rates of T-Cr gradually increase as the added amount of BPCMSs increases, and this observation is consistent with the gradually increased adsorption capacity of BPCMSs/g-C_3N_4 NSs for Cr(VI). This result indicates that Cr-containing compounds are effectively removed from water and firmly fixed on BPCMSs/g-C_3N_4 NSs after adsorption, photocatalytic reduction, and 200 °C strengthening occur. Previous XPS characterization results showed that Cr(VI) adsorbed on BPCMSs is reduced to Cr^{3+} by the photogenerated electrons because of the electron conduction effect of the graphitized BPCMSs, and Cr^{3+} is stably fixed on BPCMSs via the electrostatic interaction with surface C−OH after strengthening is performed at 200 °C (Fig. 5c and Scheme 1).

The saturated adsorption capacities of the as-prepared BPCMSs/g-C_3N_4 NSs for Cr(VI) were further investigated through the isothermal adsorption of Cr(VI) by using the as-prepared BPCMSs/g-C_3N_4 NSs at the initial aqueous Cr(VI) concentrations of 2.5, 5, 10, 20, 40, 80, 160, 240, 320, 400, and 480 mg/L. In Fig. 8c, the adsorption capacities of BPCMSs/g-C_3N_4 NSs for Cr(VI) gradually increase until saturation is reached as the initial Cr(VI) concentrations increase. The saturated adsorption capacities of the as-prepared BPCMSs/g-C_3N_4 NSs for Cr(VI) monotonically increase as the added amount of BPCMSs increases from 40 mg to 240 mg.

3.2.2. Photocatalytic degradation of aqueous organic pollutants by using the recycled Cr^{3+}/BPCMSs/g-C_3N_4 NSs

The photocatalytic performance of the recycled Cr^{3+}/BPCMSs/g-C_3N_4 NSs was further studied through the degradation of aqueous organic pollutants. The photocatalytic tests were conducted in an aqueous solution containing 10 mg/L organic pollutants without adjusting pH. In Fig. 9a, the adsorption–desorption equilibria are reached between 4-FP and the photocatalysts before they are exposed to visible light irradiation, and the direct photodegradation experiment (no catalyst) demonstrates that the change in the 4-FP concentration is negligible after 3 h of visible light irradiation. The recycled Cr^{3+}/BPCMSs(40)/g-C_3N_4 NSs exhibit the highest photocatalytic activity among all of the tested materials, and the degradation rate of aqueous 4-FP can be close to 80% after 3 h of visible light irradiation. The adsorption capacity of fresh BPCMSs(40)/g-C_3N_4 NSs for 4-FP is larger than that of the recycled Cr^{3+}/BPCMSs(40)/g-C_3N_4 NSs because the pores on BPCMSs are blocked by the loaded Cr^{3+} in Cr^{3+}/BPCMSs(40)/g-C_3N_4 NSs. However, the higher photocatalytic activity of the recycled Cr^{3+}/BPCMSs (40)/g-C_3N_4 NSs than that of fresh BPCMSs(40)/g-C_3N_4 NSs indicates that Cr^{3+} loaded on BPCMSs effectively promotes the migration of the photogenerated carriers to the surface of the g-C_3N_4 nanosheets, thereby suppressing the recombination of the photogenerated carriers inside the g-C_3N_4 nanosheets (Scheme 1). The gradually decreased photocatalytic activity of the recycled Cr^{3+}/BPCMSs(80)/g-C_3N_4 NSs and Cr^{3+}/BPCMSs(160)/g-C_3N_4 NSs compared with that of Cr^{3+}/BPCMSs(40)/g-C_3N_4 NSs suggests that excessive Cr^{3+} loading can cause the agglomeration of Cr^{3+} in BPCMSs pores, thereby reducing the

surface migration efficiency of the photogenerated carriers. g-C_3N_4 has a bulk layered structure with a low photocatalytic quantum efficiency. As such, g-C_3N_4 shows a poor photocatalytic activity for the degradation of aqueous 4-FP. The photocatalytic activity of the recycled Cr^{3+}/g-C_3N_4 is similar to that of g-C_3N_4, indicating that Cr^{3+} cannot be efficiently loaded because of the small BET specific surface area of g-C_3N_4. The photocatalytic activity of the recovered Cr(VI)/BPCMSs(40)/g-C_3N_4 NSs is also similar to that of g-C_3N_4, suggesting that Cr(VI) in $Cr_2O_7^{2-}$ cannot promote the migration of the photogenerated carriers. The 4-FP degradation rate of the recovered Cr(VI)/BPCMSs(40)/g-C_3N_4 NSs is lower than that of BPCMSs(40)/g-C_3N_4 NSs because the pores on BPCMSs are blocked by Cr(VI).

The relationship between the adsorption amount of Cr(VI) and the photocatalytic activity of the recycled Cr^{3+}/BPCMSs(40)/g-C_3N_4 NSs was further studied by changing the initial concentrations (2.5, 10, 40, 80, 160, and 320 mg/L) of aqueous Cr(VI). The systems containing Cr(VI) and BPCMSs(40)/g-C_3N_4 NSs were irradiated with visible light for 3 h after the adsorption–desorption equilibrium was reached, and a series of the recycled Cr^{3+}/BPCMSs(40)/g-C_3N_4 NSs was used for 4-FP degradation. In Fig. 9b, the photocatalytic activity of the recycled Cr^{3+}/BPCMSs(40)/g-C_3N_4 NSs gradually increases as the initial concentration of Cr(VI) increases from 2.5 mg/L to 10 mg/L. However, the photocatalytic activity of the recycled Cr^{3+}/BPCMSs(40)/g-C_3N_4 NSs gradually decreases as the initial concentration of Cr(VI) further increases to 40, 80, 160, and 320 mg/L. This result indicates that the excessively high initial concentration of Cr(VI) causes Cr^{3+} to aggregate in the BPCMSs pores, thereby reducing the separation ability of Cr^{3+} for the e^-–h^+ pairs. Similar findings have also been reported in studies on Cr^{3+}-doped TiO_2 photocatalysts [49,50].

Aqueous 4-FP was photocatalytically degraded four times to evaluate the stability of the recycled Cr^{3+}/BPCMSs/g-C_3N_4 NSs. For example, after the first catalytic run of Cr^{3+}/BPCMSs(40)/g-C_3N_4 NSs prepared at the initial Cr(VI) concentration of 10 mg/L was completed, the photocatalyst was recovered through centrifugation. The recovered photocatalyst was then used for the subsequent photocatalytic runs under the same experimental conditions. In Fig. 9c, the recycled Cr^{3+}/BPCMSs(40)/g-C_3N_4 NSs shows a considerably high stability for the photocatalytic degradation of aqueous 4-FP, and it can maintain a similar photocatalytic activity after four photocatalytic cycles. The stable photocatalytic activity of the recycled Cr^{3+}/BPCMSs/g-C_3N_4 NSs can be attributed to the firm load of Cr^{3+} on BPCMSs through the electrostatic interaction with the surface C−OH after strengthening is performed at 200 °C (Scheme 1).

The photocatalytic activity of the recycled Cr^{3+}/BPCMSs(40)/g-C_3N_4 NSs prepared at the initial Cr(VI) concentration of 10 mg/L was further evaluated by the degradation of 4-CP and 4-NP. In Fig. 9d, the gradually decreased degradation rates of the organic pollutants (4-CP > 4-FP > 4-NP) can be attributed to the gradually enhanced electron-withdrawing-induced effect of substituents (–Cl < –F < –NO₂) that lead to the gradually increasing stabilities of organic pollutants (4-CP < 4-FP < 4-NP).

3.2.3. Simultaneous photocatalytic reduction of Cr(VI) with 4-FP degradation in the combined pollution system

The photocatalytic performance of the recycled Cr^{3+}/BPCMSs/g-C_3N_4 NSs was further studied in the Cr(VI)/4-FP combined pollution system under acidic and neutral conditions by using Cr^{3+}/BPCMSs (40)/g-C_3N_4 NSs prepared at the initial Cr(VI) concentration of 10 mg/L as a representative. In Figs. 10a and b, the blank tests (no catalyst) show that the reduction of Cr(VI) and the degradation of 4-FP in the single and combined pollution systems can be disregarded. The adsorption experiments demonstrate that the adsorption–desorption equilibria between the contaminants and the photocatalyst are reached before the photocatalytic reaction occurs in either the single pollution system or the combined pollution system. In Fig. 10a, the reduction rate of Cr(VI) and the degradation rate of 4-FP are remarkably improved in the Cr
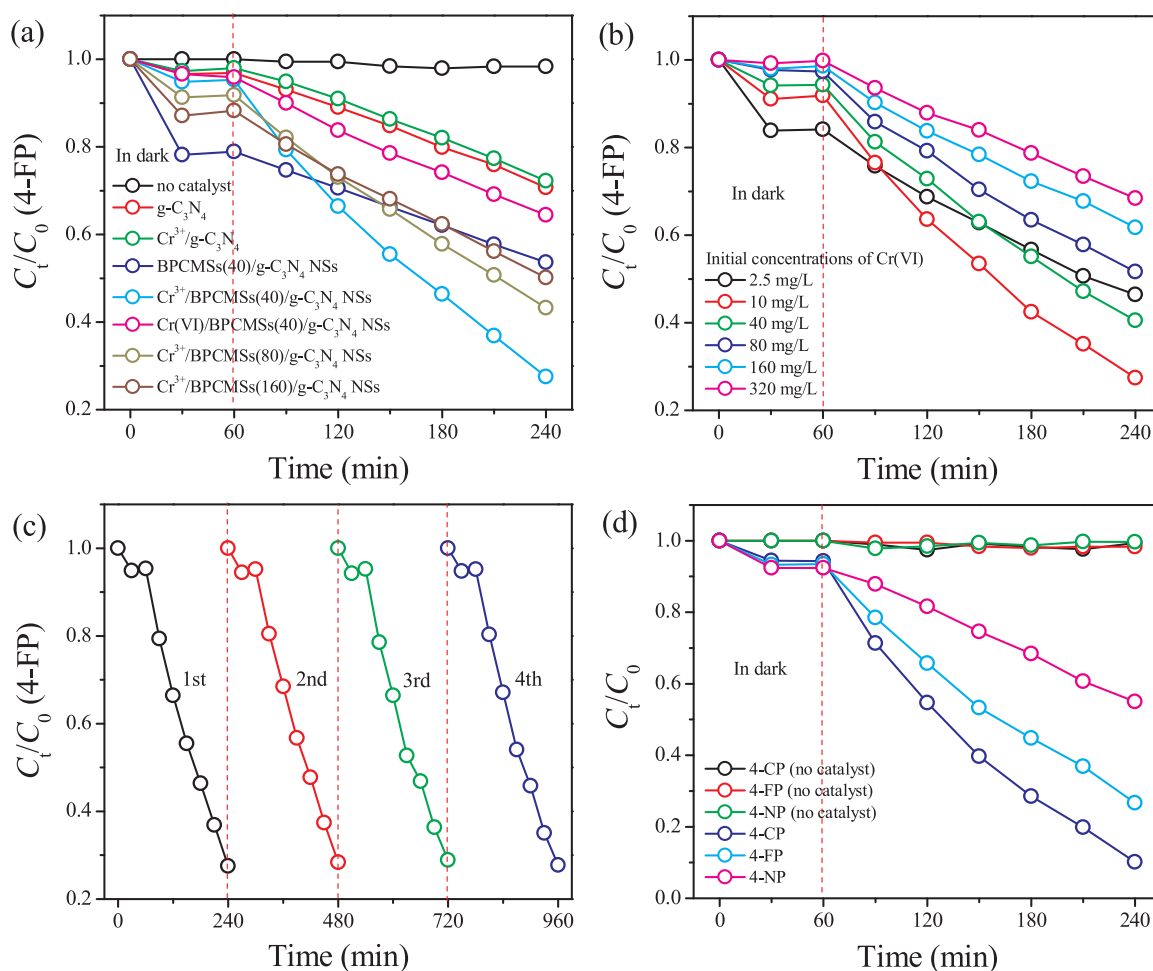
Fig. 9. Adsorption and photocatalytic degradation of aqueous 4-FP by using fresh and recycled photocatalysts (a); the relationship between adsorption amount of Cr (VI) and photocatalytic activitiy of recycled Cr^{3+}/BPCMSs(40)/g-C_3N_4 NSs (b); recycling experiments of photocatalytic degradation of aqueous 4-FP over recycled Cr^{3+}/BPCMSs(40)/g-C_3N_4 NSs (c); comparison of the photocatalytic activity of recycled Cr^{3+}/BPCMSs(40)/g-C_3N_4 NSs on the degradation of different organic pollutants (d).

(VI)/4-FP combined pollution system compared with those of the Cr(VI) or 4-FP single pollution system. This result indicates that a synergistic photocatalytic effect exists in the Cr(VI)/4-FP combined pollution system under acidic conditions. In Fig. 10b, Cr(VI) cannot be reduced by the photogenerated electrons in the Cr(VI) single pollution system because of the absence of hydrogen ions. Although the 4-FP degradation rate is slightly slowed down in the Cr(VI)/4-FP combined pollution system compared with that of the 4-FP single pollution system, the reduction of Cr(VI) is successfully carried out in the Cr(VI)/4-FP combined pollution system. That is, a synergistic photocatalytic effect also exists in the Cr(VI)/4-FP combined pollution system under neutral conditions.

The photocatalytic reaction mechanisms in the single and combined pollution systems are described as follows. We believe that a photocatalytic reaction can be smoothly carried out at different rates because the photocatalyst turns on or promotes electron transport between oxidizing and reducing agents in the photocatalytic reaction system. Specifically, the e^-–h^+ pairs are first generated through the photoexcitation of the photocatalyst. Then, the oxidizing agent is further oxidized by the photogenerated holes to form an oxidizing active intermediate (OAI), and the reducing agent is further reduced by photogenerated electrons to form a reducing active intermediate (RAI). Finally, a photocatalytic reaction is completed after the electrons transfer from the RAI to the OAI and the photocatalyst is restored to electrical neutrality (Scheme 1). In the Cr(VI) single pollution system in which pH is adjusted to 2, the RAI and the OAI are easily formed

because the electron cloud density of O atoms in $Cr_2O_7^{2-}$ is reduced by hydrogen ions. Therefore, Cr(VI) can be smoothly photocatalytically reduced under acidic conditions. In the Cr(VI) single pollution system in which pH is not adjusted, the RAI and the OAI are generated difficultly because of the high electron cloud density of O atoms in $Cr_2O_7^{2-}$. Therefore, the photocatalytic reduction of aqueous Cr(VI) is hard to carry out under neutral conditions. In the 4-FP single pollution system, the degradation rate of 4-FP under acidic conditions is slightly lower than that under neutral conditions, indicating that the presence of hydrogen ions is not conducive to the electron transport from the RAI to the OAI because of the formation of hydrofluoric acid after 4-FP is photocatalytically degraded. In the Cr(VI)/4-FP combined pollution system in which pH is adjusted to 2, the additional redox reaction between different pollutants is successfully carried out because of the electron transport from the RAI to the OAI that comes from different pollutants. Therefore, a synergistic photocatalytic effect exists in the Cr (VI)/4-FP combined pollution system under acidic conditions. In the Cr (VI)/4-FP combined pollution system in which pH is not adjusted, the redox between different pollutants is also successfully carried out because the hydrogen ions derived from 4-FP can also promote $Cr_2O_7^{2-}$ to form RAI and OAI. Therefore, Cr(VI), which cannot be photocatalytically reduced under neutral conditions, is successfully photocatalytically reduced in the neutral Cr(VI)/4-FP combined pollution system. The 4-FP degradation rate in the Cr(VI)/4-FP combined pollution system is lower than that in the 4-FP single pollution system because the competition of $Cr_2O_7^{2-}$ with the photoinduced e^-–h^+ pairs
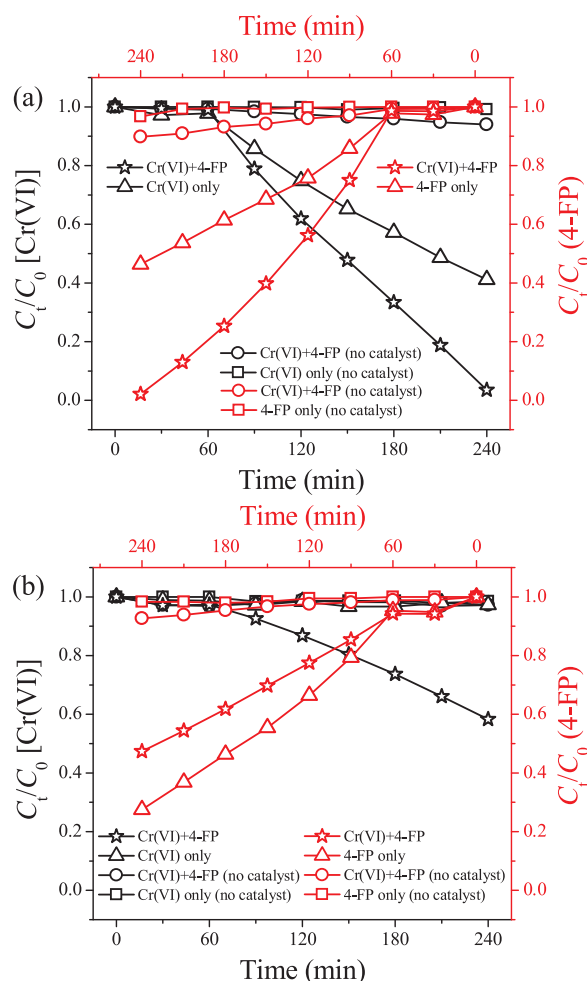
Fig. 10. Simultaneous photocatalytic reduction of Cr(VI) with 4-FP degradation in the Cr(VI)/4-FP combined pollution system by using recycled Cr^{3+}/BPCMSs (40)/g-C_3N_4 NSs under acidic (a) and neutral (b) conditions.

leads to the insufficient formation of RAI and OAI derived from 4-FP due to the high electron cloud density of O atoms in $Cr_2O_7^{2-}$ under neutral conditions.

4. Conclusions

A further calcination step can effectively remove small g-C_3N_4 in the BPCMSs pores. The as-prepared BPCMSs/g-C_3N_4 NSs exhibit large BET specific surface areas. Cr(VI) can be effectively adsorbed on the BPCMSs surface and reduced to Cr^{3+} by photogenerated electrons due to the large BET specific surface area and electron conduction effect of the graphitized BPCMSs. The photocatalytic activity of the recycled Cr^{3+}/BPCMSs/g-C_3N_4 NSs is remarkably improved compared with that of BPCMSs/g-C_3N_4 NSs for the degradation of aqueous organic pollutants because Cr^{3+} promotes the surface migration of the photogenerated carriers in the g-C_3N_4 nanosheets. The recycled Cr^{3+}/BPCMSs/g-C_3N_4 NSs show a high photocatalytic stability because Cr^{3+} is firmly loaded on BPCMSs by electrostatically interacting with surface C−OH after strengthening is performed at 200 °C. In the Cr(VI)/4-FP combined pollution system, the reduction and degradation rates of Cr(VI) and 4-FP are simultaneously enhanced under acidic conditions, and Cr(VI) is successfully reduced under neutral conditions because of synergistic photocatalytic effects.

References

[1] S. Velazquez-Peña, C. Barrera-Díaz, I. Linares-Hernández, B. Bilyeu, S.A. Martínez-Delgadillo, Ind. Eng. Chem. Res. 51 (2012) 5905–5910.
[2] X. Huang, X. Hou, F. Song, J. Zhao, L. Zhang, Environ. Sci. Technol. 50 (2016) 1964–1972.
[3] V.I. Mikhaylov, E.F. Krivoshapkina, A.L. Trigub, V.V. Stalugin, P.V. Krivoshapkin, ACS Sustain. Chem. Eng. 6 (2018) 9283–9292.
[4] Q. Hu, C. Guo, D. Sun, Y. Ma, B. Qiu, Z. Guo, ACS Sustain. Chem. Eng. 5 (2017) 11788–11796.
[5] M. Bhaumik, H.J. Choi, M.P. Seopela, R.I. McCrindle, A. Maity, Ind. Eng. Chem. Res. 53 (2014) 1214–1224.
[6] R. Zhao, X. Li, B. Sun, Y. Li, Y. Li, R. Yang, C. Wang, J. Mater. Chem. A Mater. Energy Sustain. 5 (2017) 1133–1144.
[7] D. Liu, M.W. Zhang, W.J. Xie, L. Sun, Y. Chen, W.W. Lei, Catal. Sci. Technol. 6 (2016) 8309–8313.
[8] D. Lu, P. Fang, W. Wu, J. Ding, L. Jiang, X. Zhao, C. Li, M. Yang, Y. Li, D. Wang, Nanoscale 9 (2017) 3231–3245.
[9] P. Kar, T.K. Maji, P.K. Sarkar, P. Lemmens, S.K. Pal, J. Mater. Chem. A Mater. Energy Sustain. 6 (2018) 3674–3683.
[10] C. Mondal, M. Ganguly, J. Pal, A. Roy, J. Jana, T. Pal, Langmuir 30 (2014) 4157–4164.
[11] Y. Choi, M.S. Koo, A.D. Bokare, D. Kim, D.W. Bahnemann, W. Choi, Environ. Sci. Technol. 51 (2017) 3973–3981.
[12] S. Nayak, K.M. Parida, ACS Omega 3 (2018) 7324–7343.
[13] P. Kush, K. Deori, A. Kumar, S. Deka, J. Mater. Chem. A Mater. Energy Sustain. 3 (2015) 8098–8106.
[14] D.M. Chen, C.X. Sun, C.S. Liu, M. Du, Inorg. Chem. 57 (2018) 7975–7981.
[15] J. Shang, W. Hao, X. Lv, T. Wang, X. Wang, Y. Du, S. Dou, T. Xie, D. Wang, J. Wang, ACS Catal. 4 (2014) 954–961.
[16] S. Sultana, S. Mansingh, K.M. Parida, J. Mater. Chem. A Mater. Energy Sustain. 6 (2018) 11377–11389.
[17] D.K. Padhi, A. Baral, K. Parida, S.K. Singh, M.K. Ghosh, J. Phys. Chem. C 121 (2017) 6039–6049.
[18] Y. Yang, G. Wang, Q. Deng, D.H.L. Ng, H. Zhao, ACS Appl. Mater. Interfaces 6 (2014) 3008–3015.
[19] J. Wang, X. Li, X. Li, J. Zhu, H. Li, Nanoscale 5 (2013) 1876–1881.
[20] A. Tanaka, K. Nakanishi, R. Hamada, K. Hashimoto, H. Kominami, ACS Catal. 3 (2013) 1886–1891.
[21] J. Su, Y. Zhang, S. Xu, S. Wang, H. Ding, S. Pan, G. Wang, G. Li, H. Zhao, Nanoscale 6 (2014) 5181–5192.
[22] J. Yu, S. Zhuang, X. Xu, W. Zhu, B. Feng, J. Hu, J. Mater. Chem. A Mater. Energy Sustain. 3 (2015) 1199–1207.
[23] X. Yuan, H. Wang, J. Wang, G. Zeng, X. Chen, Z. Wu, L. Jiang, T. Xiong, J. Zhang, H. Wang, Catal. Sci. Technol. 8 (2018) 1545–1554.
[24] A. Rauf, M.S.A.S. Shah, G.H. Choi, U.B. Humayoun, D.H. Yoon, J.W. Bae, J. Park, W.J. Kim, P.J. Yoo, ACS Sustain. Chem. Eng. 3 (2015) 2847–2855.
[25] F. Wu, H. Huang, T. Xu, W. Lu, N. Li, W. Chen, Appl. Catal. B: Environ. 218 (2017) 230–239.
[26] J. Zhang, X. Zhao, Y. Wang, Y. Gong, D. Cao, M. Qiao, Appl. Catal. B: Environ. 237 (2018) 976–985.
[27] H. Wang, Y. Liang, L. Liu, J. Hu, W. Cui, J. Hazard. Mater. 344 (2018) 369–380.
[28] M. Sun, Q. Zeng, X. Zhao, Y. Shao, P. Ji, C. Wang, T. Yan, B. Du, J. Hazard. Mater. 339 (2017) 9–21.
[29] T.V.M. Sreekanth, P.C. Nagajyothi, G.R. Dillip, Y.R. Lee, J. Phys. Chem. C 121 (2017) 25229–25242.
[30] S.P. Adhikari, G.P. Awasthi, H.J. Kim, C.H. Park, C.S. Kim, Langmuir 32 (2016) 6163–6175.
[31] W. Huang, N. Liu, X. Zhang, M. Wu, L. Tang, Appl. Surf. Sci. 425 (2017) 107–116.
[32] Y. Zhang, Q. Wang, J. Lu, Q. Wang, Y. Cong, Chemosphere 162 (2016) 55–63.
[33] Y. Yang, X.A. Yang, D. Leng, S.B. Wang, W.B. Zhang, Chem. Eng. J. 335 (2018) 491–500.
[34] H. Wei, Q. Zhang, Y. Zhang, Z. Yang, A. Zhu, D.D. Dionysiou, Appl. Catal. A Gen. 521 (2016) 9–18.
[35] Z. Wan, G. Zhang, X. Wu, S. Yin, Appl. Catal. B: Environ. 207 (2017) 17–26.
[36] J.C. Wang, C.X. Cui, Y. Li, L. Liu, Y.P. Zhang, W. Shi, J. Hazard. Mater. 339 (2017) 43–53.
[37] Y. Deng, L. Tang, G. Zeng, Z. Zhu, M. Yan, Y. Zhou, J. Wang, Y. Liu, J. Wang, Appl. Catal. B: Environ. 203 (2017) 343–354.
[38] J.W. Liu, Y. Luo, Y.M. Wang, L.Y. Duan, J.H. Jiang, R.Q. Yu, ACS Appl. Mater. Interfaces 8 (2016) 33439–33445.
[39] J.T. Yin, Z. Li, Y. Cai, Q.F. Zhang, W. Chen, Chem. Commun. 53 (2017) 9430–9433.

[40] K. Zhu, C. Chen, H. Xu, Y. Gao, X. Tan, A. Alsaedi, T. Hayat, ACS Sustainable Chem. Eng. 5 (2017) 6795–6802.

[41] X. Pan, Z. Liu, Z. Chen, Y. Cheng, D. Pan, J. Shao, Z. Lin, X. Guan, Water Res. 55 (2014) 21–29.

[42] Y. Yuan, S. Yang, D. Zhou, F. Wu, J. Hazard. Mater. 307 (2016) 294–301.

[43] B. Sun, E.P. Reddy, P.G. Smirniotis, Environ. Sci. Technol. 39 (2005) 6251–6259.

[44] W. Ma, K. Li, H. Guo, L. Yan, Y. Dai, X. Luo, Y. Yao, Microporous Mesoporous Mater. 250 (2017) 195–202.

[45] M. D'Arienzo, L. Armelao, C.M. Mari, S. Polizzi, R. Ruffo, R. Scotti, F. Morazzoni, J. Am. Chem. Soc. 133 (2011) 5296–5304.

[46] K. Li, Z. Zeng, L. Yan, S. Luo, X. Luo, M. Huo, Y. Guo, Appl. Catal. B: Environ. 165 (2015) 428–437.

[47] W. Xing, W. Tu, Z. Han, Y. Hu, Q. Meng, G. Chen, ACS Energy Lett. 3 (2018) 514–519.

[48] X. Li, Z. Guo, T. He, Phys. Chem. Chem. Phys. 15 (2013) 20037–20045.

[49] J. Zhu, Z. Deng, F. Chen, J. Zhang, H. Chen, M. Anpo, J. Huang, L. Zhang, Appl. Catal. B: Environ. 62 (2006) 329–335.

[50] J.C. Yu, G. Li, X. Wang, X. Hu, C.W. Leung, Z. Zhang, Chem. Commun. (2006) 2717–2719.